AIAA SciTech Forum
January 3-7, 2022, San Diego, CA & Virtual
AIAA SCITECH 2022 Forum

10.2514/6.2022-0142

Overset Adjoint-based Sensitivity Analysis for Supersonic Jet Noise

Enrico Fabiano[1], Asitav Mishra[2], Zhi Yang[1], and Dimitri Mavriplis[1]

[1]Scientific Simulations, LLC, Laramie, WY 82072-5007
[2]National Institute of Aerospace, Hampton, VA 23666

An overset, adjoint-based optimization framework for jet noise minimization is presented in this paper. The framework uses an unstructured, steady-state, Reynolds-Averaged Navier-Stokes solution for the computation of the acoustic sources in the near-field, and an acoustic-analogy approach for far-field noise propagation. An overset domain-connectivity approach is used to interface the aerodynamic solver and the acoustic software. The exact, discrete adjoint linearization of the proposed acoustic approach has been developed and verified. This multidisciplinary, adjoint-based sensitivity analysis framework is used to perform jet-noise minimization of single and multi-stream nozzle geometries.

I. Introduction

Future subsonic and supersonic airliners will have to comply with increasingly stringent community noise regulations that aim at protecting urban populations from noise pollution. Failure to meet these noise requirements, particularly during take-off and landing, could severely limit aircraft operations in the vicinity of airports and even jeopardize the aircraft certification effort. During landing and take-off operations, the aircraft noise signature is dominated by airframe, fan and jet noise. Among these noise sources, jet noise is of particular interest because of the intrinsically multidisciplinary nature of the nozzle design optimization problem. The optimal nozzle design must comply with stringent noise regulations at subsonic speeds, while producing the thrust required to sustain supersonic flight. Hence, the objective of the this work is the development and demonstration of an efficient numerical optimization strategy for the aeroacoustic design of the next generation of commercial supersonic nozzles.

While first-principle CFD methods such as Large Eddy Simulation (LES) methods for the prediction of jet noise offer great accuracy, the high computational cost of these approaches make their application to noise design minimization problems impractical. On the other hand, despite suffering from reduced accuracy, acoustic-analogy approaches based on steady-state RANS CFD solvers can predict noise design trends at a fraction of the cost of first principle approaches and can be employed in design optimization studies. In the present work we propose an acoustic-analogy approach based on the NSU3D RANS CFD solver[1] and on the NASA JeNo_v3 jet-noise code.[2–4] In this approach the unstructured NSU3D flow solver is used to compute the steady RANS solution around a nozzle geometry. The unstructured CFD solution is then interpolated on the structured grid used by the JeNo_v3 code to compute the far-field noise spectra for the nozzle. The interpolation of the RANS solution is performed using the TIOGA[5] overset domain connectivity algorithm. Furthermore, after successful computation of the far-field noise levels, the noise spectra can be used by the NASA ANOPP2 software[6,7] to compute the certification noise metrics for the nozzle. Additionally, in order to enable the gradient-based sensitivity analysis of the proposed jet-noise prediction strategy, in this work we have developed the exact adjoint linearization of the coupled jet-noise analysis approach by developing the exact discrete adjoint of the JeNo_v3 code and coupling it to the adjoint linearizations of the NSU3D CFD solver, and the sensitivity analysis capability of the NASA ANOPP2 code. A schematic of the proposed acoustic-analogy approach and of its linearization is shown in Fig. 1. Upon verification of the implemented sensitivities, the adjoint linearization of our jet-noise prediction framework has been used to perform the gradient-based noise minimization of single and multi-stream nozzles.

The rest of the paper is structured as follows: Section II discusses the aerodynamic solver and its adjoint linearization, while Section III describes the TIOGA overset domain-connectivity algorithm and its linearization. Section IV presents the acoustic formulation and the verification of the adjoint linearization implemented in this work. Section V presents the optimization results. Finally, Section VI draws conclusions and highlights possible future work.

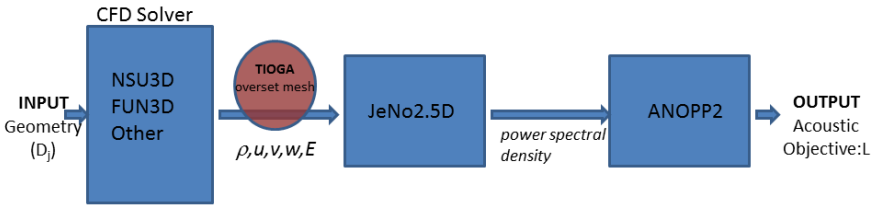

(a) Analysis

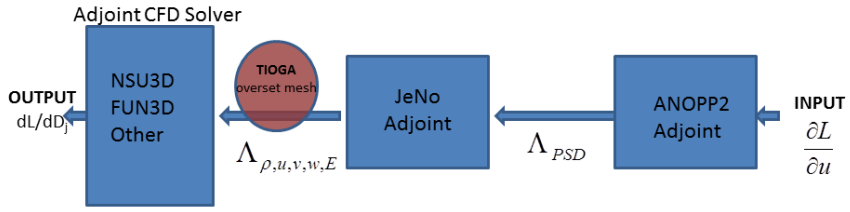

(b) Adjoint

Figure 1. Illustration of flow of information for analysis and adjoint of coupled aeroacoustic problems

II. Aerodynamic Analysis and Sensitivity Formulation

A. Flow Solver Analysis Formulation

The base flow solver used in this work is the NSU3D unstructured mesh Reynolds-averaged Navier-Stokes solver. NSU3D has been extensively applied to steady-state and time-dependent flows and contains a discrete tangent and adjoint sensitivity capability. Hence, only a concise description of these formulations will be given in this paper, with additional details available in previous references.[1,8–10] The flow solver is based on the conservative form of the Navier-Stokes equations which may be written as:

$$\frac{\partial \mathbf{U}(\mathbf{x},t)}{\partial t} + \nabla \cdot \mathbf{F}(\mathbf{U}) = 0 \tag{1}$$

where the state vector $\mathbf{U}$ consists of the conserved variables and the Cartesian flux vector $\mathbf{F} = (\mathbf{F}_x, \mathbf{F}_y, \mathbf{F}_z)$ contains both inviscid and viscous fluxes. The equations are closed with the perfect gas equation of state and the $k-\omega$ turbulence model[11,12] for all cases presented in this work. The solver uses a vertex-centered median dual control volume formulation that is second-order accurate, where the flux integral around a closed control volume is discretized as:

$$\mathbf{R}(\mathbf{U}) = \sum_{\mathbf{dB(t)}} [\mathbf{F}(\mathbf{U})] \cdot \mathbf{ndB} = \sum_{\mathbf{i=1}}^{\mathbf{n_{edge}}} \mathbf{F}^{\perp}_{\mathbf{e_i}}(\mathbf{U}, \mathbf{n_{e_i}}) \mathbf{B_{e_i}} = \mathbf{0} \tag{2}$$

where B_e is the face area, $\mathbf{n}_e$ is the unit normal of the face, and $F_e^{\perp}$ is the normal flux across the face. The normal flux across the face is computed using a second-order accurate matrix dissipation scheme[13] as the sum of a central difference and an artificial dissipation term. For the case of steady-state flows considered in this work, the time derivative term in equation (1) represents a pseudo-time term used to facilitate convergence to the steady-state solution. After the residual vector $\mathbf{R}$ is linearized with respect to the unknown flow solution vector $\mathbf{U}$, the system of nonlinear equations (2) is solved using a quasi-Newton scheme. The Jacobian matrix is inverted iteratively using a line-implicit agglomeration multigrid scheme that can either be sued directly as a linear solver or can be applied as a preconditioner for a GMRES Krylov solver.[14]

The flow around the SMC006 nozzle[15] is used to validate the NSU3D flow solver for jet-flow applications. The nozzle is axisymmetric and is augmented with 6 triangular chevrons. The flow conditions correspond to Set Point 7 from the Tanna Matrix.[16] The nozzle pressure ratio is $p_0/p_\infty = 1.861$, the temperature ratio $T_0/T_\infty = 1$ and the jet Mach number is $M_j = 0.985$. A freestream Mach number $M_\infty = 0.01$ is imposed as a freestream boundary condition to facilitate the convergence of the flow solver[17] and the Reynolds number based on the freestream Mach number for this $2in$ diamater nozzle is $Re = 5789.0/in$. The unstructured CFD mesh used to simulate the flow around the nozzle

is shown in Fig. 2(a). The mesh consists of approximately 2.34 million nodes and is refined near the nozzle exit to better resolve the jet shear layer. The nozzle aerodynamic performance prediction has been validated in our previous work.[18] For instance, a comparison between computed and experimental[15] contours of total pressure coefficient at several streamwise stations is reproduced from previous work in Fig. 2. The validated aerodynamic analysis is an essential step towards accurate prediction of noise metrics using JeNo.

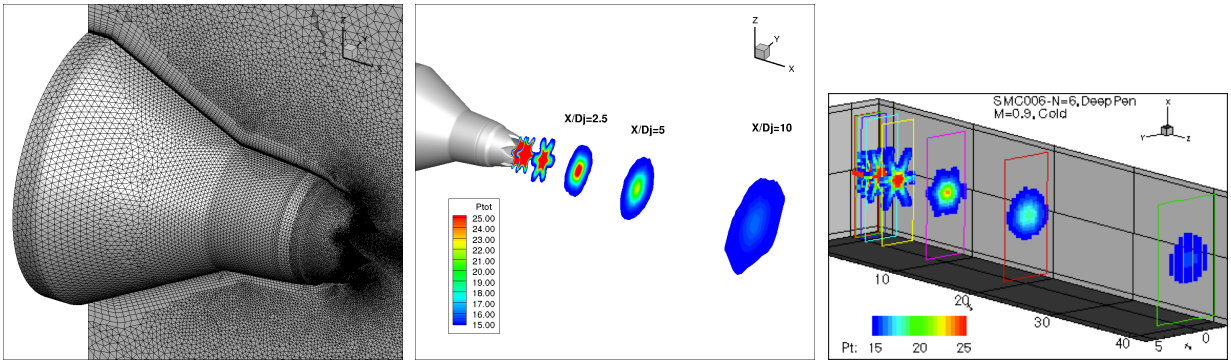

(a) Unstructured CFD mesh

(b) Contours of computed total pressure coefficient at different streamwise stations

(c) Contours of experimental total pressure coefficient at different streamwise stations[15]

Figure 2. Validation of the NSU3D $k-\omega$ computations for the SMC006 nozzle geometry[18]

B. Mesh deformation capability

In order to apply shape changes computed by the optimization algorithm, a mesh deformation strategy must be employed. In this approach, the mesh is modeled as a linear elastic solid with a variable modulus of elasticity that can be prescribed either as inversely proportional to cell volume or to the distance of each cell from the nearest wall.[19,20] The resulting equations are discretized and solved on the mesh in its original undeformed configuration in response to surface displacements using a line-implicit multigrid algorithm analogous to that used for the flow equations. The governing equations for mesh deformation can be written symbolically as:

$$\mathbf{G}(\mathbf{x}, \mathbf{x_{surf}}(\mathbf{D})) = \mathbf{0} \tag{3}$$

where $\mathbf{x}$ denotes the interior mesh coordinates and $\mathbf{x_{surf}}(\mathbf{D})$ are the surface mesh coordinates that depend on the shape parameters that define the surface geometry.

C. Aerodynamic Sensitivity Analysis Formulation

The sensitivity analysis implementation follows the strategy developed in references.[1,8] The objective function L is evaluated using the steady flow and mesh solution, $\mathbf{U}$ and $\mathbf{x}$ respectively, as:

$$L = L(\mathbf{U}, \mathbf{x}) \tag{4}$$

Assuming that the state variables, i.e., $\mathbf{U}, \mathbf{x}$, are dependent on some input design parameters $\mathbf{D}$, the total sensitivity of the objective function L to a design variable D can be expressed as the inner product between the vector of state sensitivities to the design input and the vector of objective sensitivities to the state variables as:

$$\frac{dL}{dD} = \begin{bmatrix} \frac{\partial L}{\partial \mathbf{x}} & \frac{\partial L}{\partial \mathbf{U}} \end{bmatrix} \begin{bmatrix} \frac{d\mathbf{x}}{dD} \\ \frac{d\mathbf{U}}{dD} \end{bmatrix} \tag{5}$$

The non-linear flow residual operator and the linear elasticity mesh residual operator described earlier provide the constraints for the sensitivity analysis:

$$\begin{aligned} \mathbf{G}(\mathbf{x}, \mathbf{D}) &= 0 \\ \mathbf{R}(\mathbf{U}, \mathbf{x}) &= 0 \end{aligned} \tag{6}$$

and their linearization with respect to the design variable yields:

$$\begin{bmatrix} \frac{\partial \mathbf{G}}{\partial \mathbf{x}} & 0 \\ \frac{\partial \mathbf{R}}{\partial \mathbf{x}} & \frac{\partial \mathbf{R}}{\partial \mathbf{U}} \end{bmatrix} \begin{bmatrix} \frac{d\mathbf{x}}{dD} \\ \frac{d\mathbf{U}}{dD} \end{bmatrix} = \begin{bmatrix} -\frac{\partial \mathbf{G}}{\partial D} \\ 0 \end{bmatrix} \tag{7}$$

Upon solution of the forward sensitivity equation (7), the mesh and flow sensitivity vectors can be substituted into equation (5) to obtain the complete sensitivity of the objective L with respect to the design variable D. Hence, the forward sensitivity approach requires a new solution of equation (7) for each design parameter D. On the other hand, the adjoint approach can obtain the sensitivities for any number of design inputs $\mathbf{D}$ at a cost approximately independent of the number of design variables. The adjoint formulation can be obtained by transposing the tangent linearization in equation (7), resulting in equation (8)

$$\begin{bmatrix} \frac{\partial \mathbf{G}}{\partial \mathbf{x}}^T & \frac{\partial \mathbf{R}}{\partial \mathbf{x}}^T \\ 0 & \frac{\partial \mathbf{R}}{\partial \mathbf{U}}^T \end{bmatrix} \begin{bmatrix} \Lambda_{\mathbf{x}} \\ \Lambda_{\mathbf{U}} \end{bmatrix} = \begin{bmatrix} \frac{\partial L}{\partial \mathbf{x}}^T \\ \frac{\partial L}{\partial \mathbf{U}}^T \end{bmatrix} \tag{8}$$

where $\Lambda_{\mathbf{U}}$ and $\Lambda_{\mathbf{x}}$ are the flow and mesh adjoint variables respectively. The final objective sensitivities can then be obtained as:

$$\frac{dL}{d\mathbf{D}}^T = \begin{bmatrix} \frac{\partial \mathbf{G}}{\partial \mathbf{D}}^T & 0 \end{bmatrix} \begin{bmatrix} \Lambda_{\mathbf{x}} \\ \Lambda_{\mathbf{u}} \end{bmatrix} \tag{9}$$

A more detailed description of the complete formulation can be found in reference.[1]

III. TIOGA Overset Interface: Analysis and Sensitivity Formulation

To perform the acoustic analysis, the farfield noise spectra is computed by interpolating an unstructured steady RANS solution onto the structured grid employed by the acoustic propagation tool. The grid connectivities between the overset structured and unstructured grids are handled through the TIOGA interface (Topology Independent Overset Grid Assembler).[5,21] TIOGA performs so-called implicit hole cutting on both the meshes and executes the fringe cell interpolation between them. TIOGA is a high performing assembler as it makes use of an efficient parallel implementation of the Alternating Digital Tree (ADT)[22] for point-cell inclusion tests. In essence, TIOGA provides the cell donor-receptor information as well as the interpolation coefficients between the overset grids.

Development of an adjoint-based optimization framework necessitates linearization of the TIOGA overset method. Therefore, in this work, adjoint linearization of TIOGA has been implemented and verified with respect to its tangent linearization. The following sections discuss the TIOGA interpolation, its linearization as well as its verification.

A. RANS-JeNo Interface: TIOGA Interpolation and Linearization

The TIOGA overset framework provides the interface between the CFD RANS (NSU3D) and the acoustic (JeNo) modules. The solution information from the CFD unstructured grid needs to be propagated on to the JeNo structured grid as shown in Figure 3. This interpolation can be written as:

$$\mathbf{U}_{JeNo} = [T(\mathbf{x}_{JeNo}, \mathbf{x}_{RANS}(\mathbf{D}))]\,\mathbf{U}_{RANS} \tag{10}$$

where, $\mathbf{U}_{RANS,JeNo}$ are flowfield solutions on the RANS unstructured and JeNo structured meshes, respectively, $\mathbf{x}_{RANS}(\mathbf{D})$ represents the unstructured mesh coordinates, which depend on the nozzle shape design parameters $\mathbf{D}$, and $\mathbf{x}_{JeNo}$ denotes the coordinates of the JeNo structured mesh, which are fixed. Here T represents the interpolation matrix. The tangent linearization of Eqn. (10) with respect to the design variables D can be written as:

$$\frac{d\mathbf{U}_{JeNo}}{d\mathbf{D}} = T\frac{d\mathbf{U}_{RANS}}{d\mathbf{D}} + \frac{\partial T}{\partial \mathbf{x}_{RANS}}\frac{d\mathbf{x}_{RANS}}{d\mathbf{D}}\mathbf{U}_{RANS} \tag{11}$$

Here, the first term on the right-hand side simply corresponds to the direct interpolation of the RANS *solution sensitivities* onto the JeNo mesh. The second term in Eqn. 11 contains the sensitivities arising from RANS *mesh sensitivities* that translate into the TIOGA *interpolation coefficient sensitivities*. The term $\frac{\partial T}{\partial \mathbf{x}_{RANS}}$, in essence, is what we refer to as the TIOGA tangent linearization. The mesh sensitivities arise from the RANS mesh deformation in response to the design shape changes of the nozzle. Finally, note that the JeNo mesh does not deform with the nozzle and thus has no dependence on the design variables D. Similarly, the adjoint linearization is given as:

$$\begin{aligned} \Lambda_{\mathbf{U}_{RANS}} &= T^{Tr}\Lambda_{\mathbf{U}_{JeNo}} \\ \Lambda_{\mathbf{x}_{RANS}} &= \left[\frac{\partial T}{\partial \mathbf{x}_{RANS}}\right]^{Tr}\Lambda_{\mathbf{U}_{JeNo}}\mathbf{U}_{RANS} \end{aligned} \tag{12}$$

Here, $\Lambda_{\mathbf{U},\mathbf{x}}$ terms are the analogous adjoint variables which are of the same dimension as the corresponding forward sensitivity variables (i.e. $\frac{d\mathbf{U}}{dD}$ and $\frac{d\mathbf{x}}{dD}$.) Figure 3(a) shows the RANS unstructured grid which is depicted as the shaded domain with defined boundaries, such as, *inlet, nozzle wall, free stream BCs*. Figure 3(b) shows the cylindrical structured JeNo grid. TIOGA is utilized to obtain the donor cells from the unstructured RANS (NSU3D) mesh for each of the the structured (JeNo) grid nodes. Figure 4 shows the RANS and JeNo interface grid system. Fig. 4(a)

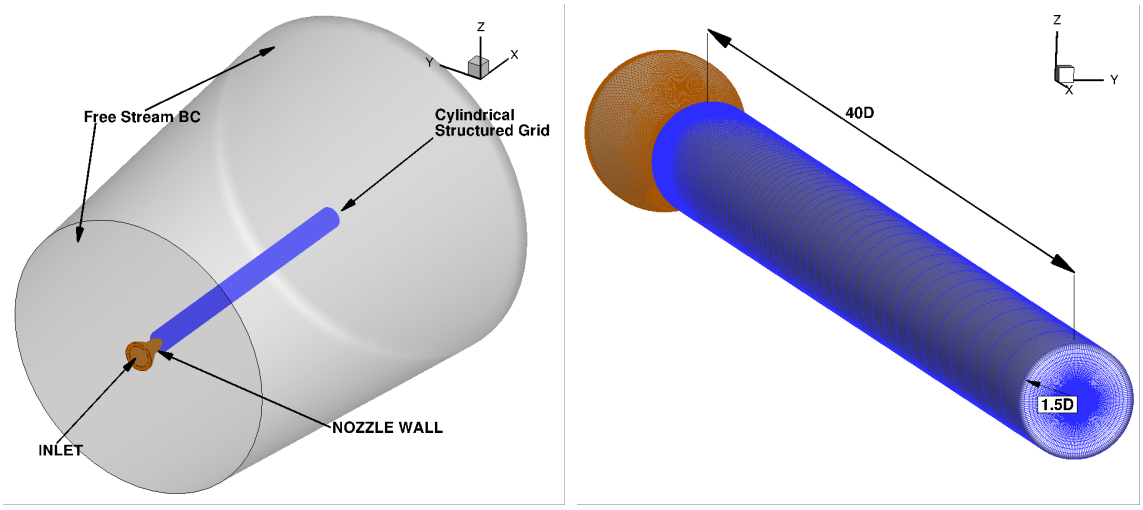

(a) Computational domain (b) JeNo grid

Figure 3. RANS and JeNo computational interface

illustrates how the RANS donor cells (in brown) interpolate (linearly) the computed solution onto the JeNo grid nodes (in blue). In this case, we want the solution computed on the unstructured CFD grid to be interpolated onto the entire JeNo structured grid. Therefore, the impicit hole cutting algorithm in TIOGA is over-ridden and all JeNo grid nodes are forced to be fringe nodes (iblank = -1) as shown in Fig. 4(b). In this work we have used tri-linear interpolation, but higher order accurate interpolation routines are also available in TIOGA which may be investigated in future.

B. TIOGA Analysis and Sensitivity Verification

Figures 5 shows the nozzle flowfield solution on the JeNo grid interpolated from the RANS unstructured grid. The flow conditions correspond to Setpoint 7 from Tanna et al.[16] Figure 5(a) shows Mach contours at several stream-wise planes. For the plane at ($X = 0.5D$) (where D is the nozzle exit diameter) shown in Figure 5(b), the solution contours plotted on the JeNo strutured grid are qualitatively almost identical to the solution contours plotted on the unstructured RANS CFD grid. These interpolation results demonstrate that the TIOGA domain connectivity algorithm provides an effective and accurate strategy for the interpolation of an unstructured RANS solution onto a JeNo structured mesh, allowing for the efficient prediction of the noise generated by complex nozzle geometries.

To verify the tangent and adjoint sensitivities of the overset methodology, an objective function is constructed that accounts for the TIOGA sensitivities. The objective function employs an approximate-acoustic analogy developed in previous work, which uses a simplified JeNo noise computation[18] method. The notable modification to the noise

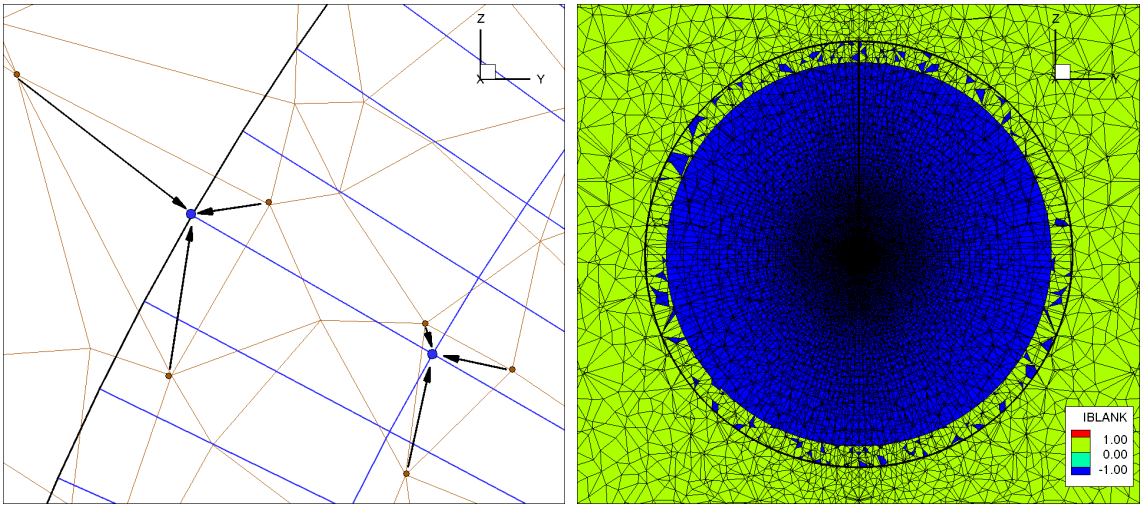

(a) RANS donor cells for JeNo fringe points (b) Iblank values for RANS and JeNo grids

Figure 4. RANS and JeNo overset interface

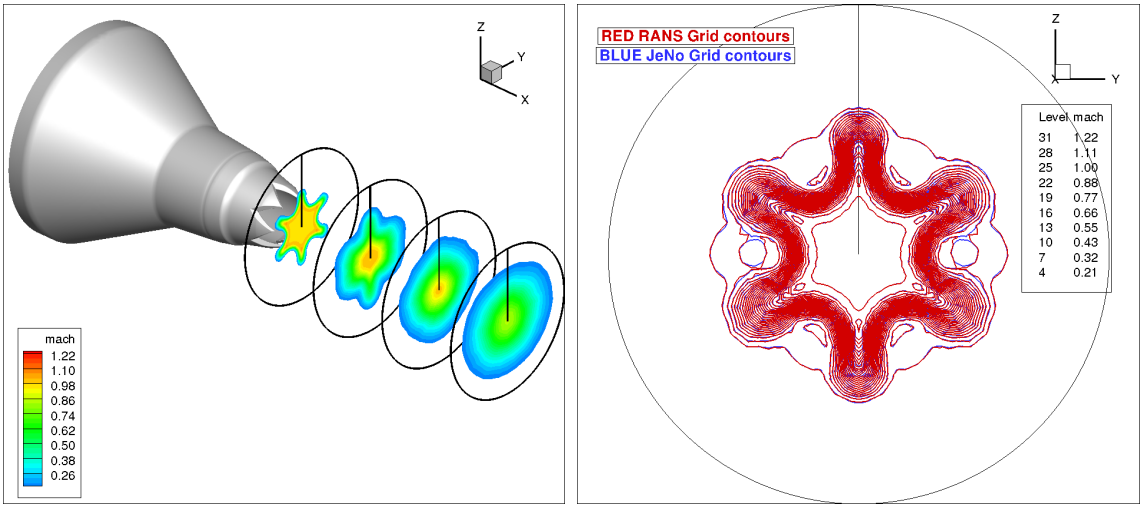

(a) JeNo Grid Contours (b) X=0.5D plane contours comparison

Figure 5. Interpolated Mach contours of the JeNo grid

objective computation compared to the previous work is that it is now computed using the cylindrical structured mesh solution *interpolated* from the nozzle unstructured mesh solution instead of computing it using the nozzle mesh directly. This cylindrical mesh used is already shown in Figure 3(b). This approach serves as a stepping stone to the development of the fully coupled NSU3D, TIOGA and JeNo adjoint-linearized modules. The approximate-acoustic objective sensitivities thus constructed are used to verify the TIOGA overset framework.

As shown in our previous work,[18] the aero-acoustic objective function is composed of the noise objective with an aerodynamic objective as a constraint enforced using a penalty function formulation:

$$L_{tot} = L_{acou} + \omega_{aero} L_{aero} \tag{13}$$

$$L_{acou} = \sum_{\omega^s} PSD(\omega^s) \tag{14}$$

$$L_{aero} = (Cd - Cd_{baseline})^2 \tag{15}$$

where $Cd_{baseline}$ is the drag coefficient of the baseline SMC006 nozzle and $\omega_{aero} = 1.0 \times 10^{-6}$ is a penalty weight used to enforce the aerodynamic constraint. *PSD* is the jet noise source term radiated to the far field, and integrated over the structured cylindrical mesh.

Again, Fig. 3 shows the overset computational domain composed of the nozzle unstructured mesh and the cylindrical structured mesh, with a total of 4.5 million nodes, considered for the objective sensitivity verification study. The structured cylindrical mesh has $161 \times 71 \times 181$ nodes along the stream-wise, radial and azimuthal directions (1 plane every 2°), respectively, and thus a total of about 2 million nodes. The nozzle unstructured polyhedral mesh contains approximately 2.5 million nodes. For this test case, the flow conditions are given by Set Point 7 from the Tanna Matrix,[16] with a nozzle pressure ratio $\frac{p_o}{p_\infty} = 1.861$, a temperature ratio $\frac{T_o}{T_\infty} = 1$ and a jet Mach number $M_j = 0.985$. Table 1 shows the tangent and adjoint sensitivities, which agree to machine precision for a given nozzle shape parameter (chevron penetration). The sensitivity agreement with the finite difference method is also reasonable, although better agreement using different step sizes remains to be investigated.

Table 1. *Objective Sensitivity Verification in TIOGA overset framework*

	dL_{tot}/dD
Finite Difference	0.349400909982478e-04
Tangent	0.361478951904**47**E-04
Adjoint	0.361478951904**68**E-04

IV. Coupled CFD-CAA Methodology

Despite the continuous increase in computational resources, jet-noise design-optimization strategies based on scale-resolving acoustic-analogy approaches are still infeasible. A viable approach to nozzle design optimization is the use of RANS-based hybrid methods that have been developed over the years and are now fairly well established.[2,4,23–25] These hybrid methods use a finely resolved near-field steady RANS solution to predict the noise radiated from the jet to a given observer using an acoustic-analogy formulation. The acoustic formulation proposed in this work is based on the JeNo_v3 software[2,4,23] and is capable of predicting the far-field noise spectra for both cold and hot jets using the RANS solution computed by the NSU3D CFD solver. Additionally, the proposed acoustic formulation is coupled to the ANOPP2 software[6,7] to enable the computation of certification noise metrics of the jet.

For gradient-based nozzle shape optimization, the discrete adjoint linearization of the JeNo_v3 software was developed and implemented in this work and coupled to the linearization of the flow solver to compute the sensitivity of the acoustic objective function with respect to the full vector of design variables. Finally, minimization of the certification noise metrics computed by ANOPP2 was enabled by coupling the adjoint linearizations of the NSU3D CFD solver and the JeNo_v3 code to the sensitivity analysis path in the NASA ANOPP2 software.[7]

A. Jet-Noise Predictions using JeNo_v3 and ANOPP2

Based on Lilley's acoustic analogy, the JeNo code computes the noise sources of the jet from a structured RANS solution following the approach described in references.[2,4] The structured grid covers the entire jet-plume region

downstream of the nozzle exit. A Green's function approach is then used to propagate the noise spectra to the far-field observers. For observers at right angles from the nozzle axis the computation of the propagation filter is relatively straight-forward. However, for acoustic observers located at general angles from the nozzle axis, the computation of the Green's function requires the numerical integration of a stiff, second-order ordinary differential equation (ODE).[2] The solution of the ODE is computed using an adaptive algorithm that adjusts both the order of accuracy and the step size of the numerical integration, and the high computational cost of this integration strategy results in computationally expensive jet-noise predictions for observers at general angles from the nozzle axis. Finally, upon successful computation of the far-field noise levels, the noise spectra can be harnessed by the ANOPP2 software[6,7] to compute the certification noise metrics for the jet.

For the jet-noise prediction strategy proposed in this work, the unstructured RANS solutions computed with the NSU3D flow solver are interpolated onto JeNo's structured mesh using the TIOGA overset domain connectivity algorithm,[5,21] and shared memory pointers are used to provide the interpolated solution to the JeNo jet-noise code for far-field propagation.

A validation of the acoustic analogy approach implemented in this work is shown in Fig. 6. The steady RANS solution around the SMC006 nozzle[15] has been computed using the NSU3D flow solver using the unstructured grid and flow conditions described in section A. The CFD unstructured surface grid and the JeNo structured grid are shown in Fig. 6(a). The JeNo mesh consists of a 120-degree section of a cylindrical grid, and is centered at the nozzle axis. The grid extends two nozzle diameters in the radial direction and 40 nozzle diameters downstream of the nozzle exit, with 81 nodes in the radial and axial directions and 61 nodes in the azimuthal direction. The acoustic observer is placed 40 equivalent nozzle diameters from the nozzle exit, at 90 degrees from the nozzle axis.[15] The noise spectra at the

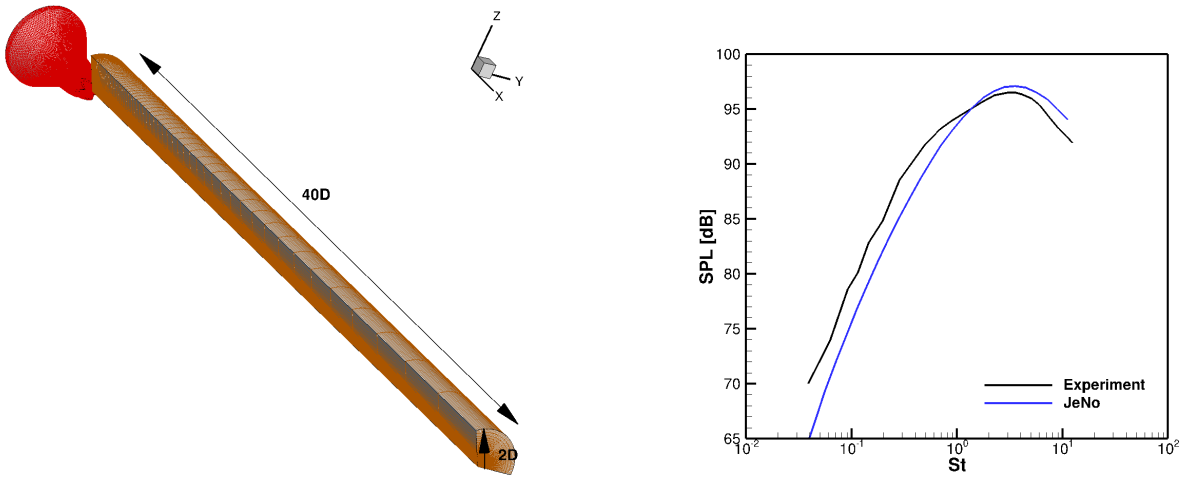

(a) Unstructured surface grid and JeNo's structured grid used for the demonstration of the implemented adjoint-based sensitivity analysis framework.

(b) Comparison of experimental and numerical 1/3-octave spectrum for a 90-degree observer.

Figure 6. JeNo's structured grid and comparison between predicted and computed noise spectra for the baseline SMC006 nozzle.

observer are shown in Fig. 6(b). There is reasonable agreement between computed and measured spectra, establishing confidence in both the NSU3D CFD solution and the 'NSU3D-TIOGA-JeNo' noise prediction strategy.

Additionally, the noise spectra propagated by JeNo have been used to compute the certification noise metrics using the ANOPP2[6,7] acoustic software. Table 2 shows Perceived Noise Level (PNL) and tone-corrected Perceived Noise Level (PNLT) for the SMC006 nozzle with a 90-degree observer. The coupling between JeNo and ANOPP2 is realized through shared memory pointers

Table 2. *Certification metrics for the SMC006 chevron nozzle. The tone correction is negligible for this jet-noise prediction*

PNL	110.99
PNLT	110.99

1. *MPI parallelization*

In order to improve the run time of jet-noise prediction and sensitivity analysis, particularly for observers at general angles from the nozzle axis, in this work we developed a parallel version of the the JeNo_v3 code based on the domain-decomposition approach. In this approach, the JeNo structured mesh is divided into multiple subdomains, and the contribution of each subdomain to the far-field noise spectra is computed in parallel by different compute cores. The MPI protocol is used to compute the total noise spectra by summing the contributions from all the compute cores. The JeNo structured mesh is partitioned by grouping together grid planes normal to the jet axis, as shown in Fig. 7(a). Figure 7(b) shows the computational performance of the parallel version of the JeNo_v3 code. The domain-

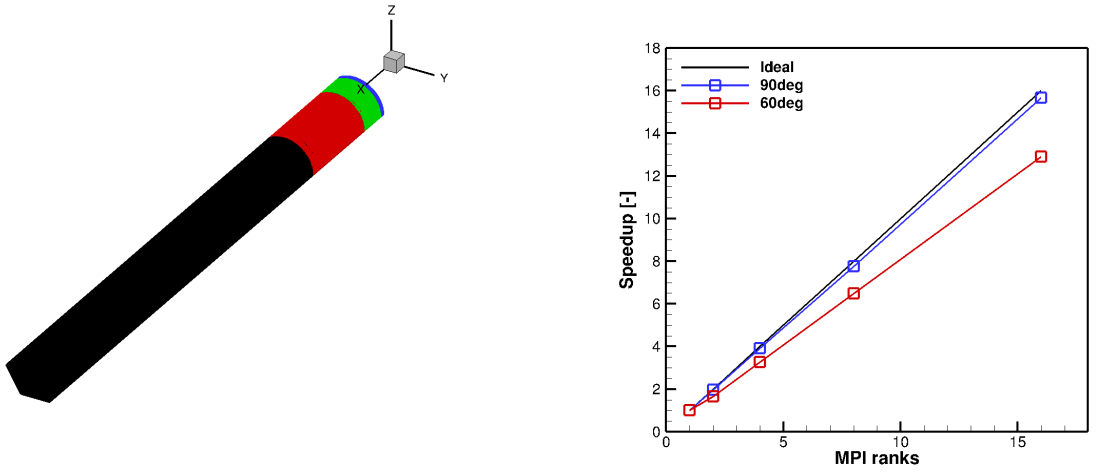

(a) JeNo structured grid partitioned across four MPI ranks

(b) Computational performance of the parallel version of the JeNo_v3 code

Figure 7. JeNo_v3 MPI parallelization

decomposition strategy significantly reduces the run time for the sensitivity analysis of a noise prediction at general observers enabling efficient adjoint-based nozzle shape optimization. For the 90 degree observer case, near perfect scalability is observed up to 16 processors. For the general observer case, scalability is slightly lower. This is due to the load imbalance between processors which arises due to the fact that the adaptive ODE integrator can take different paths (order of accuracy and time step sizes) on different processors. However, the overall speedups are still only slightly lower than optimal.

B. Adjoint-based sensitivity analysis for jet noise

In order to enable gradient-based nozzle shape optimization for jet noise, in this work the JeNo source code has been augmented with its exact discrete adjoint linearization following the approach described in.[1] The acoustic objective function used for verification of the sensitivities is the OASPL acoustic metric as computed by JeNo, while Perceived Noise Level (PNL) is the acoustic objective function used to validate the linearization of the JeNo_v3-ANOPP2 coupling. JeNo's tangent linearization has been verified using both the finite-difference approach and the complex-step method. In the finite-difference approach, the nozzle geometry has first been perturbed by changing the penetration of a design variable that describes the shape of the nozzle. Then, the RANS solutions computed by NSU3D on both the baseline and the perturbed nozzle geometries have been interpolated onto the same JeNo structured mesh using the TIOGA overset domain connectivity algorithm. Finally, upon propagation of the two solutions through JeNo, the sensitivity of OASPL with repect to the penetration design variable has been computed with a one-sided, first-order finite-difference formula. For the tangent method, the two interpolated solutions have been finite-differenced using the same first-order, one-sided finite difference formula to form the forward sensitivity input vector of the mean-flow and turbulence solutions with respect to the perturbed design variable. This forward sensitivity has then been propagated through the tangent linearization version of JeNo. For the complex step method, this forward input sensitivity vector is added as an imaginary component to the input state vector of JeNo, which is now run in the complex variable mode of JeNo implemented specifically for sensitivity verification. Following the complex step method, the imaginary part of the output objective of JeNo yields the complex-step value of the objective sensitivity. This verification exercise

has been performed for a single-stream and a multi-stream nozzle for different locations of the acoustic observer. The single-stream jet is the SMC006 nozzle,[15] and the flow conditions correspond to Set Point 7 in the Tanna matrix,[16] the CFD solution has been computed on the unstructured grid described in Section A, while the JeNo structured mesh has been described in the previous section. The acoustic observer is placed 40 equivalent nozzle diameters from the nozzle exit, at different angles from the nozzle axis.[15] Table 3 shows the sensitivity of OASPL and thrust of the nozzle computed by the adjoint-enhanced JeNo_v3 code for this cold jet case, for an observer at 90 degrees, and there is excellent agreement among JeNo's complex, tangent and adjoint linearizations, and reasonable agreement with the finite-difference computed sensitivities. Furthermore, in order to enable the gradient-based sensitivity analysis of the certification noise metrics computed by ANOPP2 with respect to the design variables in the CFD model, the adjoint linearizations of the CFD solver, of the JeNo code and of the ANOPP2 software have been coupled via shared memory pointers. Table 4 shows the sensitivity of PNL computed by the coupled JeNo_v3-ANOPP2[6,7] framework with respect to chevron penetration for the SMC006 nozzle. Here, there is excellent agreement among the tangent and adjoint linearizations, and all the implemented sensitivities agree with the finite-difference method to the ninth significant digit. Sensitivity comparisons with the complex step method using ANOPP2 were not possible since we did not have access to the complexified version of ANOPP2. Table 5 compares tangent and adjoint sensitivities with respect to chevron penetration for observers at 60 and 150 degrees from the nozzle axis to the sensitivities computed with the finite-difference method for this cold jet case. Here again we obtain close to machine precision equivalence between the tangent and adjoint sensitivities, as expected. The agreement with finite difference values is reasonable, although less precise than in the 90 degree observer case. In the finite difference sensitivity calculation, we speculate that the perturbation in the input vector is large enough to cause the adaptive ODE integration scheme to take a slightly different path in terms of step size and order of accuracy at each integration step. A smaller perturbation in the finite-difference scheme may be expected to yield results closer to the tangent/adjoint values, although sensitivity values computed using smaller perturbations become swamped with roundoff error due to the conditioning of the Green's function integration. Note that the complex-step method cannot be applied for the general observer case since the original JeNo source code of the Green's function integration involves complex variables itself. Nevertheless,

Table 3. *Verification of JeNo's linearization for an observer at 90 degrees by comparison with the complex-step method*

	OASPL	Thrust
Finite Difference	6.2238**9990212469**00	13.86**93399875933**
Complex	6.223865642714**4856**	13.8686296088024
Tangent	6.223865642715**1546**	13.8686296088029
Adjoint	6.223865642715**1824**	13.8686296088021

Table 4. *Sensitivity of Perceived Noise Level computed with ANOPP2 with respect to chevron penetration*

Finite Difference	18.790529**1682000654**
Tangent	18.7905294022**902076**
Adjoint	18.7905294022**881578**

Table 5. *Verification of JeNo's linearization by comparison with the finite-difference method for observers at 60 and 150 degrees from to the nozzle axis*

	60deg	150deg
Finite difference	**7.22859994084502**	18.**3294999089867**
Tangent	5.375161041**54010**	18.917121877**9490**
Adjoint	5.375161041**52310**	18.917121877**9541**

the agreement between tangent and adjoint sensitivities provides evidence that the implementation is correct and the agreement with finite difference is deemed sufficient for design optimization purposes.

After verification of the implemented sensitivities on a cold, single-stream nozzle, the tangent and adjoint linearizations of the JeNo_v3 software have also been verified for the case of a multi-stream hot jet. This multi-stream jet consists of a round nozzle that surrounds the SMC006 geometry described in the previous sections. The RANS CFD solution is computed using the NSU3D flow solver on an unstructured mesh consisting of approximately 2.5 million grid nodes, as shown in Fig. 8(a). The flow conditions are described in Table 6, and a freestream Mach number of $M_\infty = 0.01$ is used to facilitate convergence of the CFD solver, while the Reynolds number is the same as in the single-stream SMC006 nozzle case. Figure 8(b) shows the contours of Mach number for the flow around the multi-

Table 6. *Core and bypass boundary conditions for the multi-stream nozzle*

	Core	Bypass
p/p_0	1.85	1.85
T/T_0	3.2	1.2

stream nozzle computed with the NSU3D flow solver. The acoustic observer is placed 40 inner-nozzle diameters from the nozzle axis, at 90 degrees. The JeNo structured grid is shown in Fig. 8(c) and consists of a 120-degree section of a cylindrical mesh. The JeNo grid is centered at the nozzle axis and extends 40 inner-nozzle diameters downstream of the nozzle axis, and 4 outer-nozzle diameters in the radial direction, with 151 nodes in the streamwise direction, 141 nodes in the radial direction and 61 nodes in the azimuthal direction. Table 7 shows the sensitivity of OASPL

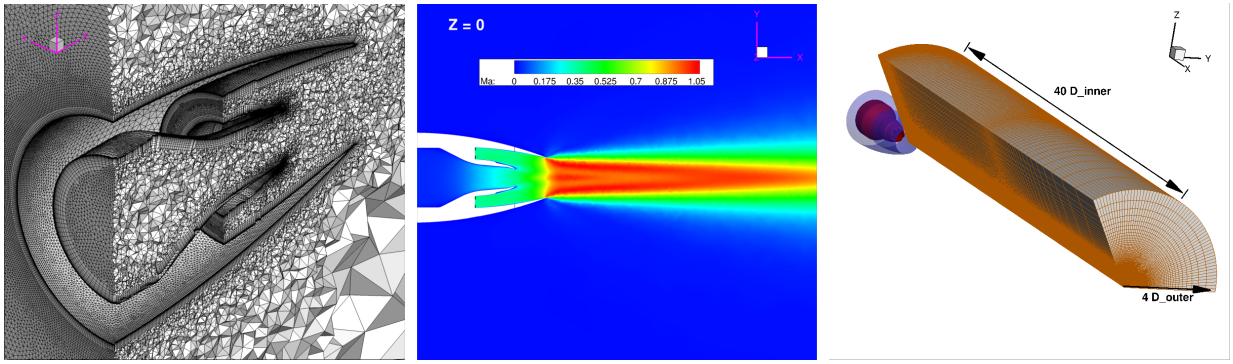

(a) Unstructured CFD mesh for the multi-stream nozzle

(b) Mach contour for the multi-stream, hot jet

(c) Multi-stream nozzle geometry and JeNo's structured grid used for the demonstration of the implemented adjoint-based sensitivity analysis framework.

Figure 8. Nozzle geometry and JeNo strucutred grid for the multi-stream, hot-jet case.

Table 7. *Verification of JeNo's linearization for an observer at 90 degrees by comparison with the finite-difference and the complex-step method for the hot-jet case*

	Hot jet
Finite difference	-44.4082**00210455164**
Complex	-44.408255397**81830**
Tangent	-44.408255397**81654**
Adjoint	-44.408255397**93468**

computed by the adjoint-enhanced JeNo-v_3 software with respect to penetration of the outer nozzle. The implemented tangent and adjoint sensitivites are compared to both the finite-difference and the complex-step approach. The

implemented sensitivities agree to the 6th significant figure with the finite-difference approach, and to the 12th significant figure with the complex-step approach, confirming the correctness of the tangent and adjoint sensitvities of the JeNo_v3 code.

V. JeNo-based Design Optimizations

The NSU3D-TIOGA-JeNo-ANOPP2 adjoint-based sensitivity analysis framework that has been developed in the course of this project is used here to perform shape optimizations of single and multi-stream nozzles. The goal of the optimizations is to reduce the far-field noise signature of the nozzle without compromising its propulsive performance. The optimization problem is formulated as

$$\min_{\mathbf{D}} L_{Tot} \tag{16}$$

where the objective function is

$$L_{Tot} = \omega_{Acou} L_{Acou} + \omega_{Thrust} L_{Thrust} \tag{17}$$

The acoustic objective function in Eqn (17) is either the Overall Sound Pressure Level (OASPL) computed by JeNo or the Perceived Noise Level (PNL) computed by ANOPP2 using the noise spectrum computed by JeNo, and $\omega_{acou} = 1$. The propulsive objective function is

$$L_{Thrust} = \left(Thrust - Thrust_{baseline}\right)^2 \tag{18}$$

where $Thrust$ is the nozzle thrust computed by JeNo_v3 at the nozzle exit, $Thrust_{baseline}$ is the thrust of the baseline nozzle as computed by JeNo, and ω_{Thrust} is a penalty weight.

A. Single-stream Nozzle Optimization

For the single-stream nozzle, the vector of design variables **D** consists of chevron penetration, twist and nozzle length, as shown in Figure 9. For each optimization, one design cycle corresponds to one flow solution and one adjoint solution, and is computed on 144 compute cores. The flow and adjoint solutions around the nozzle are computed using 144 cores, while the noise spectra are computed by JeNo using 16 cores. Each design cycle takes approximately 30 and 60 minutes for the 90 and 60 degree observer cases, respectively.

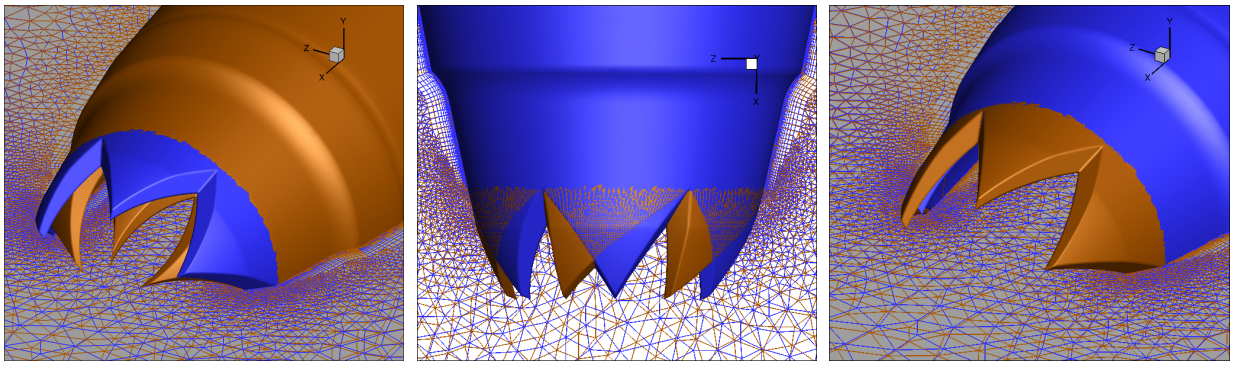

(a) Chevron penetration (b) Chevron twist (c) Nozzle length

Figure 9. Nozzle design variables; Blue: baseline, Orange: deformed

1. *OASPL optimization for a 90deg observer*

For this optimization $\omega_{Thrust} = 0$ in Eqn. (17) and the acoustic objective function is the OASPL computed by JeNo for a 90-degree observer, $L_{acou} = OASPL$. Convergence of the optimization is shown in Fig. 10 After 10 design cycles, optimality is reduced one order of magnitude, with the acoustic objective function experiencing its most significant reduction in only two design cycles. This optimization results in approximately a 1dB reduction of OASPL, and

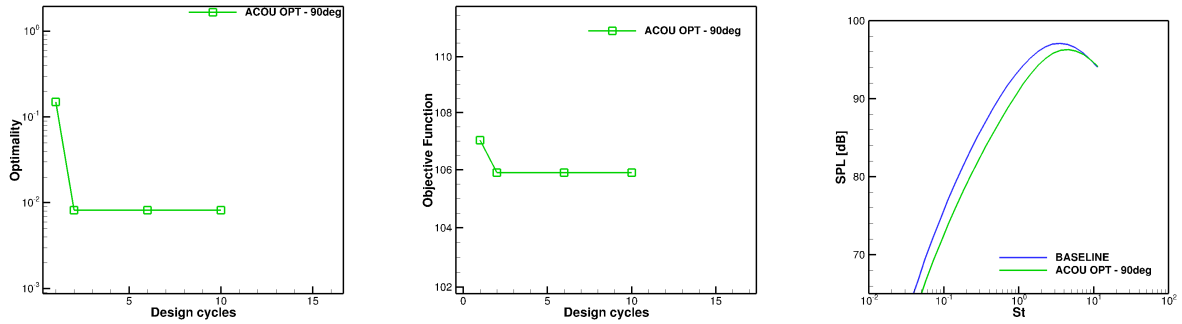

(a) Optimality (b) Objective (c) Noise

Figure 10. Convergence of the acoustic optimization for a 90-degree observer: a) Optimality as computed by SNOPT, b) optimization objective as function of design cycles, and c) comparison of baseline and optimized acoustic spectra

a comparison of the noise spectra for the baseline and optimized nozzle is shown in Figure 10(c). However, the noise reduction comes with a 13.5% thrust reduction, highlighting the conflicting propulsive and acoustic design requirements. A comparison between the baseline and optimized nozzle shape is shown in Figure 11. The noise reduction is achieved with increased chevron penetration in agreement with previous experimental and computational design studies,[15,26] while chevron twist and nozzle length play a minimal role in the optimization.

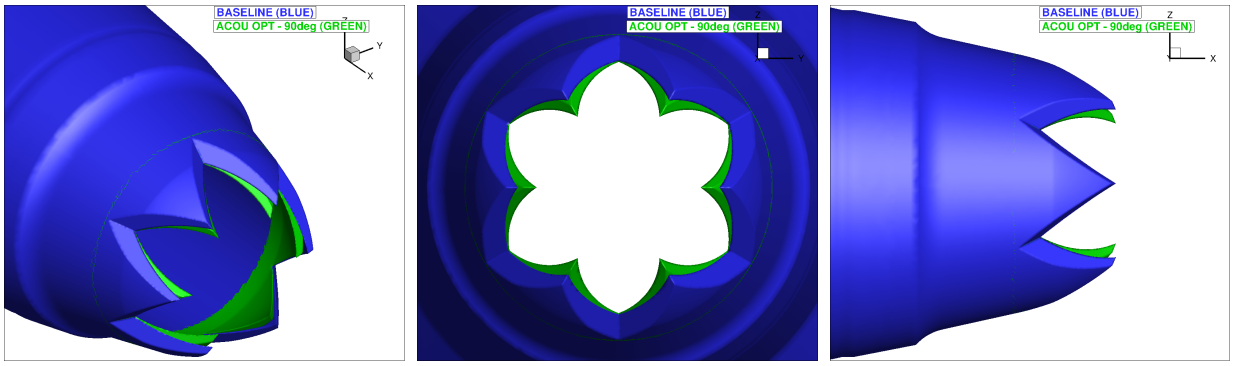

(a) Deformed geometry (b) Deformed geometry - top view (c) Deformed geometry - side view

Figure 11. Nozzle shapes for the baseline and optimized nozzles, acoustic optimization (OASPL), 90deg observer

2. *PNL optimization for a 90deg observer*

For this optimization $\omega_{Thrust} = 0$ in Eqn. (17) and the acoustic objective function is PNL computed by ANOPP2 for a 90-degree observer, $L_{acou} = PNL$. Hence, this optimization employs the entire NSU3D-TIOGA-JeNo-ANOPP2 adjoint-based sensitivity-analysis approach developed in this project. Convergence of the optimization problem is shown in Fig. 12 After 10 design cycles, optimality is reduced three orders of magnitude, with the acoustic objective function experiencing its most significant reduction in only two design cycles. This optimization results in approximately a 3dB PNL reduction, and a comparison of the noise spectra for the baseline and optimized nozzle is shown in Fig. 12(c). However, similar to the OASPL optimization presented in the previous section, the noise reduction comes with a 13.5% thrust reduction. A comparison between the baseline and optimized nozzle shape is shown in Figure 13. Furthermore, a comparison between the OASPL and PNL optimized nozzle is shown in Fig. 14. The two optimizations result in similar nozzle shapes and the noise spectra of the two nozzles are indistinguishable, confirming that noise reduction is achieved mainly by increasing chevron penetration.

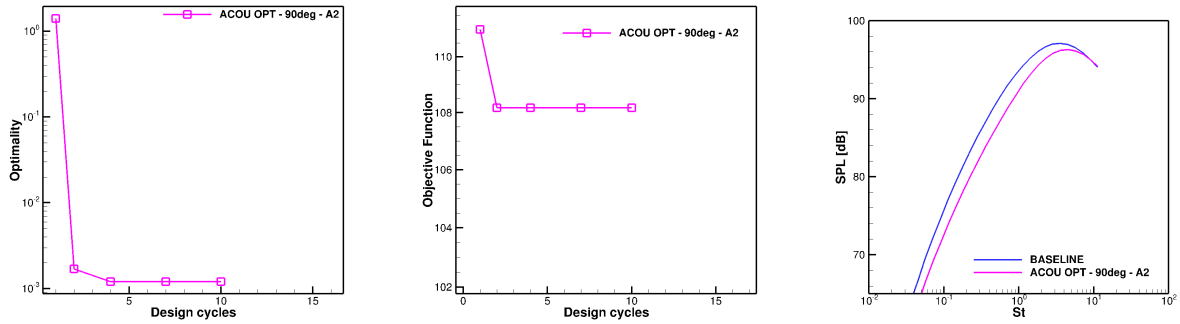

(a) Optimality (b) Objective (c) Noise

Figure 12. Unconstrained acoustic optimization (PNL) convergence and noise spectra

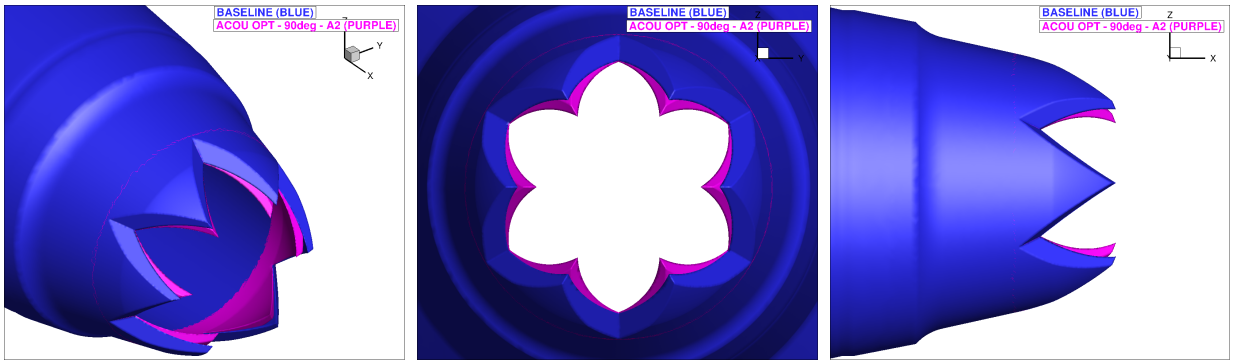

(a) Deformed geometry (b) Deformed geometry - top view (c) Deformed geometry - side view

Figure 13. Nozzle shapes for the baseline and optimized nozzles, acoustic optimization (PNL), 90deg observer

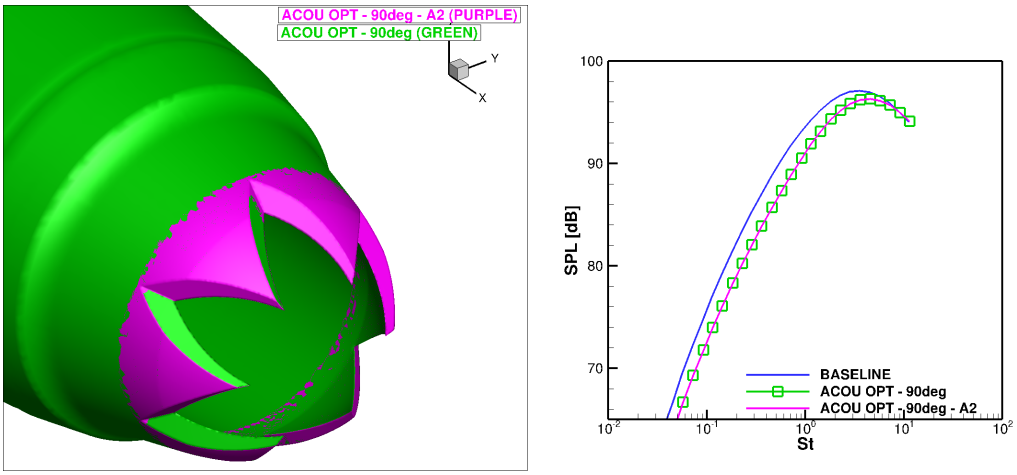

(a) Nozzle geometries (b) Noise spectra at 90 degree

Figure 14. Comparison of OASPL and PNL optimized nozzles (A2 denotes ANOPP2 objective: PNL)

3. Aeroacoustic optimization for a 90deg observer

For this optimization $\omega_{acou} = 1$ and $\omega_{Thrust} = 0.075$ in eq. (16). Convergence of the optimization problem is shown in Fig. 15 and is achieved after 11 design cycles. The optimization results in an OASPL reduction of approximately

0.6dB and Fig. 15(c) compares the noise spectra for the baseline nozzle, the OASPL-optimized nozzle and the nozzle designed with the aeroacoustic optimization presented in this section. Similar to the previous optimizations, the noise reduction is achieved with increased chevron penetration, while the twist and length design variables play a more limited role, as shown in Figure 16. Finally, the nozzle thrust decreases only by 6.6%, as a result of weakly enforcing the aerodynamic constraint through the penalty function approach of Eqn (16).

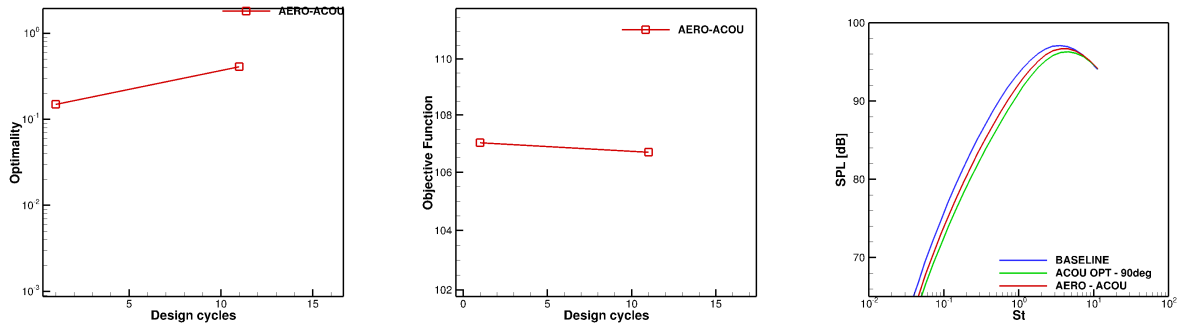

(a) Optimality (b) Objective (c) Noise

Figure 15. Aeroacoustic optimization convergence and noise spectra for a 90 deg observer

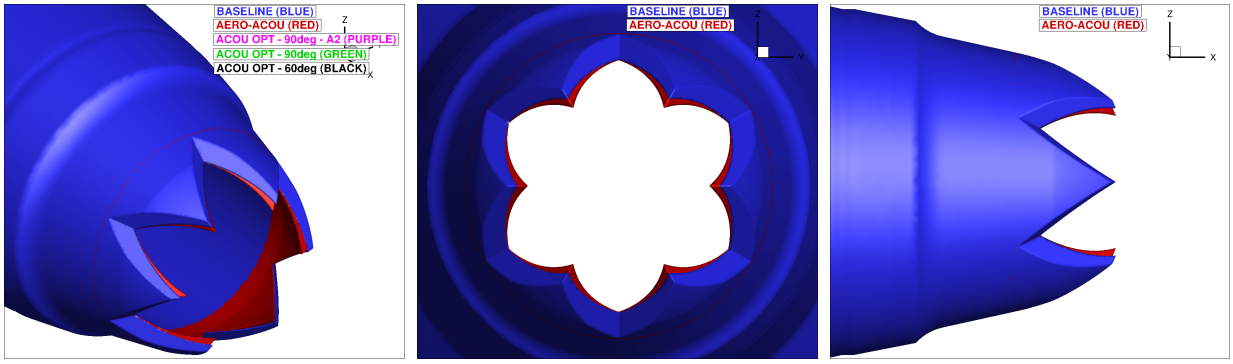

(a) Deformed geometry (b) Deformed geometry - top view (c) Deformed geometry - side view

Figure 16. Nozzle shapes for the baseline and optimized nozzles, aeroacoustic optimization, 90deg observer

4. OASPL optimization for a 60deg observer

The final optimization performed is the unconstrained noise minimization of the SMC006 nozzle for an observer at 60 degrees from the nozzle axis. For this optimization $\omega_{Thrust} = 0$ in Eqn. (17) and the acoustic objective function is OASPL as computed by JeNo_v3 for the 60-degree observer, with $L_{acou} = OASPL$. Convergence of the optimization is shown in Figure 17. After 16 design cycles, optimality is reduced by two orders of magnitude, with the acoustic objective function experiencing its most significant reduction in only two design cycles. This optimization results in approximately a 1dB reduction of OASPL, and a comparison of the noise spectra for the baseline and optimized nozzle is shown in Fig. 17(c). Similar to the previous OASPL and PNL optimizations, the noise reduction comes with a 13.5% thrust reduction. Finally, a comparison between the baseline and optimized nozzle shape is shown in Fig. 18. The noise reduction is achieved with increased chevron penetration, while chevron twist and nozzle length play a minimal role in the optimization, similar to the 90-degree observer case. Figure 19 shows a comparison of the 90-degree and 60-degree observer OASPL-optimized nozzle shapes. The similar nozzle shapes highlight the fact that the design space is somewhat limited to a strong dependence on chevron penetration for this test case.

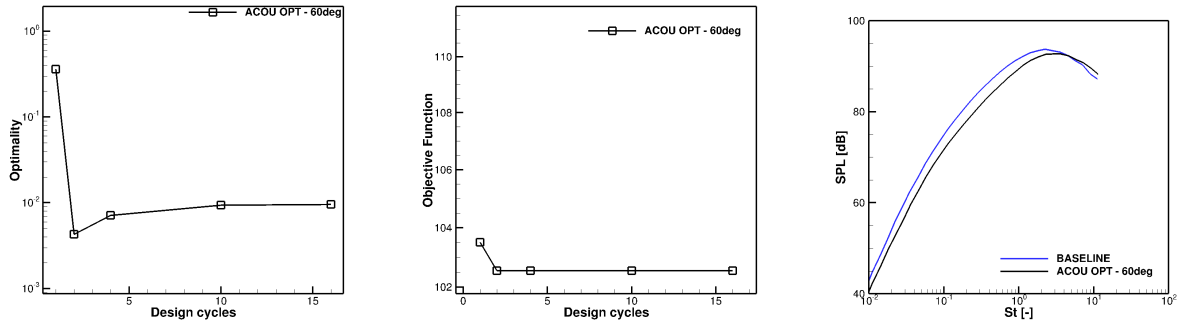

(a) Optimality (b) Objective (c) Noise

Figure 17. Unconstrained acoustic (OASPL) optimization convergence and noise spectra for a 60 deg observer

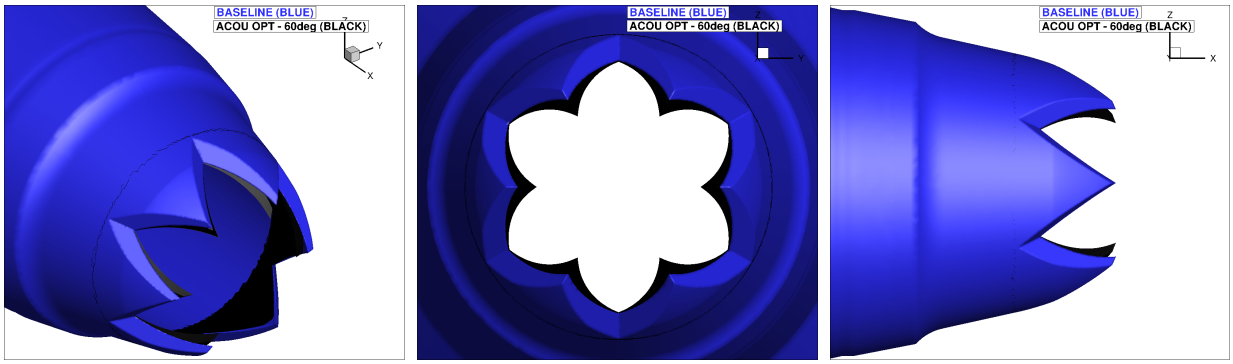

(a) Deformed geometry (b) Deformed geometry - top view (c) Deformed geometry - side view

Figure 18. Nozzle shapes for the baseline and optimized nozzles, aeroacoustic optimization, 60deg observer

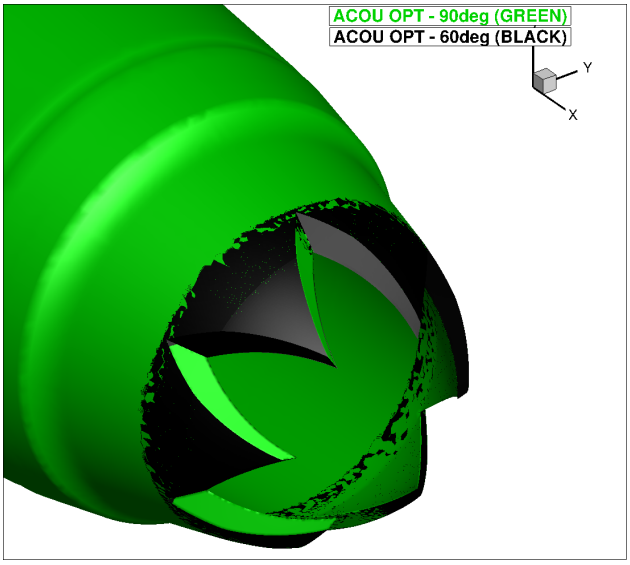

Figure 19. Comparison of nozzles shapes for the 90-degree and 60-degree OASPL optimizations.

B. Multi-stream Nozzle Optimization

The coupled adjoint CFD/CAA sensitivity formulation was further extended for optimization of a multi-stream nozzle configuration, where additional design shape parameters are included. This configuration uses the SMC006 nozzle discussed in the previous section for the core stream, with an outer nozzle geometry enclosing the SMC006 nozzle creating a bypass flow stream. The unstructured CFD mesh and the JeNo structured grid for this optimization are similar to those described in the multi-stream nozzle sensitivity verification Section. IV and shown in Fig. 8. However, this case involves cold streams and the geometry is slightly modified from the previous configuration, with an area ratio of approximately 6. The flow conditions for the core and the bypass streams are described in Table 8. The acoustic

Table 8. Core and bypass boundary conditions for the multi-stream nozzle

	Core	Bypass
p/p_0	1.85	1.2
T/T_0	1.0	1.0

observer is placed at 40 equivalent nozzle diameters from the nozzle exit at 90 degrees from the nozzle axis. For this optimization $\omega_{THRUST} = 0$ and the acoustic objective function is the the Overall Sound Pressure Level (OASPL) computed by JeNo. The vector of design variables $\mathbf{D}$ consists of a combination of design variables for the inner and the outer nozzles. The design variables for the inner SMC006 nozzle are chevron penetration, twist and nozzle length, as shown in Figure 9. For the outer nozzle, the design variables are nozzle penetration and nozzle length, as shown in Fig. 20.

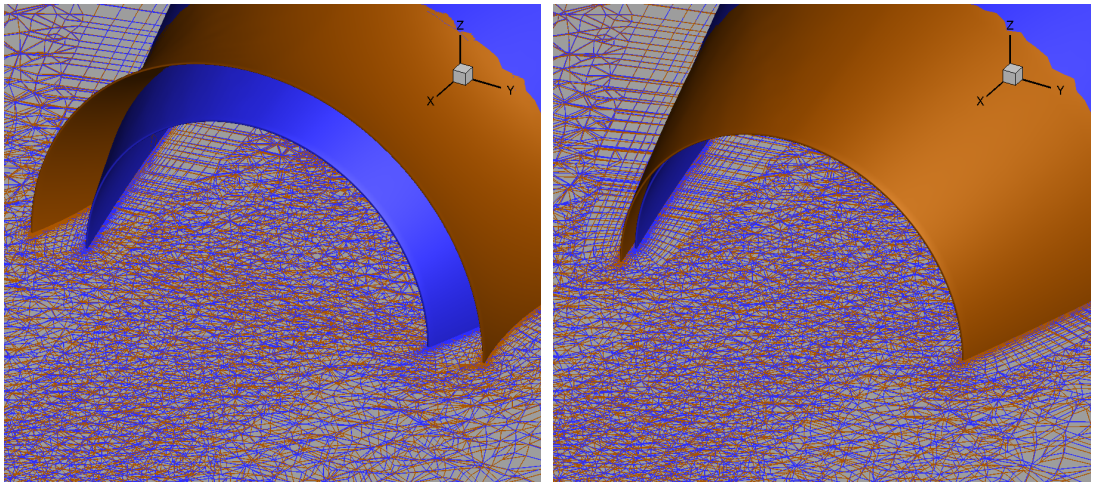

(a) Outer nozzle penetration (b) Outer nozzle length

Figure 20. Design variables for the multi-stream nozzle; Blue: baseline, Orange: deformed

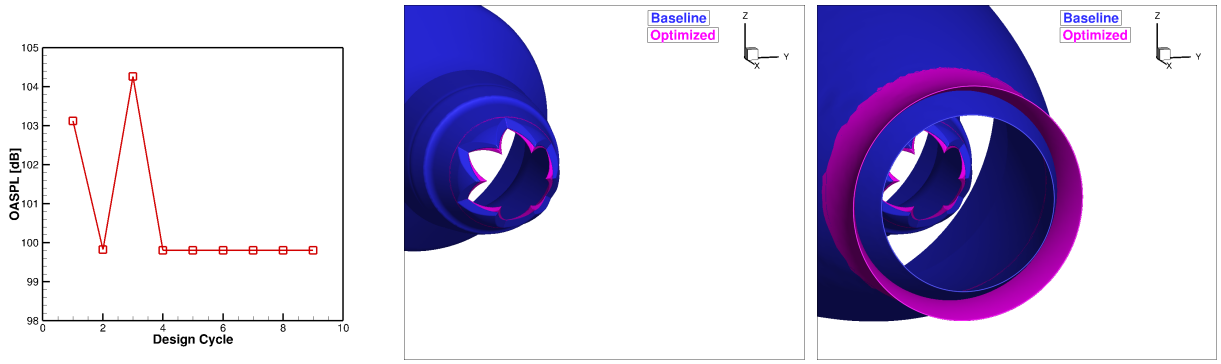

(a) Objective function convergence (b) Inner nozzle (c) Both inner and outer nozzles

Figure 21. Convergence of the optimization problem for the multi-stream nozzle and comparison between baseline and optimized geometry

For each optimization, one design cycle corresponds to one flow solution and one adjoint solution, and is computed on 144 compute cores. The flow and adjoint solutions around the nozzle are computed using 128 cores, while the noise spectra are computed by JeNo using 16 cores. Each design cycle takes approximately 45 minutes. Convergence of the optimization problem is shown in Fig. 21(a). The objective function settles after 5 design cycles and results in 3.3dB reduction in OASPL. The noise reduction is achieved predominantly by increasing the penetration of the chevron of the inner nozzle and decreasing penetration of the outer nozzle, as shown in Fig. 21(b) and Fig. 21(c).

VI. Conclusions

In this work we have developed and validated an adjoint-enhanced acoustic-analogy approach. This approach is based on a steady-state Reynolds-averaged Navier-Stokes (RANS) solver and on the NASA JeNo and ANOPP2 software, which are coupled to the unstructured mesh RANS CFD solver using an overset domain-connectivity approach. The acoustic analogy and its exact adjoint linearization have been developed using tight in-memory coupling between the RANS solver and the NASA JeNo and ANOPP2 codes, and the coupled software suite runs seamlessly and efficiently on parallel computer architectures. The adjoint computed sensitivities have been verified to machine precision for the case of a 90 degree observer. For the general observer case, machine precision agreement between tangent and adjoint sensitivities was obtained. However, verification with the complex-step method was not possible due to the use of complex variables in this path of the JeNo code. Reasonable agreement with finite-difference values was observed, although the stiff nature of the Green's function integration for the general observer case along with the adaptive ODE integration used in JeNo was found to hinder exact sensitivity agreement. Upon verification, the implemented adjoint sensitivities have been used to perform the noise minimization of a single stream nozzle and a multi-stream nozzle. The optimizations highlight the conflicting acoustic and propulsive design requirements. Future work should focus on expanding the design space for multi-stream nozzles through the judicious choice of relevent shape design paramenters.

VII. Acknowledgements

The authors would like to acknowledge support of NASA through NASA SBIR 2018 Phase-II funding, Contract: 80NSSC19C0090, Proposal: 18-2-A1.04-5483.

References

[1]Mavriplis, D. J., "Discrete Adjoint-Based Approach for Optimization Problems on Three-Dimensional Unstructured Meshes," *AIAA Journal*, Vol. 45-4, April 2007, pp. 741–750.

[2]Khavaran, A., Bridges, J., and Georgiadis, N., "Prediction of Turbulence-Generated Noise in Unheated Jets. Part 1: JeNo Technical Manual," NASA/TM 2005-213827.

[3]Khavaran, A., Wolter, J. D., and Koch, D. L., "Prediction of Turbulence-Generated Noise in Unheated Jets. Part 2: JeNo User's Manual (Version 1.0)," NASA/TM—2009-213827/PART2.

[4]Khavaran, A. and Bridges, J., "An Empirical Temperature Variance Source Model in Heated Jets," NASA/TM 2012-217743.

[5]Roget, B. and Sitaraman, J., "Robust and efficient overset grid assembly for partitioned unstructured meshes," *Journal of Computational Physics*, Vol. 260, 2014, pp. 1–24.

[6]Lopes, L. and Burley, C., "Design of the next generation aircraft noise prediction program: ANOPP2," *AIAA Paper 2011-2854, 17th AIAA/CEAS Aeroacoustics Conference*, Portland, OR, June 5–8 2011, p. 2854.

[7]Lopes, L. V., Iyer, V. R., and Born, J., "Robust Acoustic Objective Functions and Sensitivities in Adjoint-Based Design Optimizations," *AIAA Paper 2017-1673, 55th AIAA Aerospace Sciences Meeting*, Grapevine, TX, January 9–13 2017.

[8]Mavriplis, D. J., "Solution of the Unsteady Discrete Adjoint for Three-Dimensional Problems on Dynamically Deforming Unstructured Meshes," *AIAA Paper 2008–0727, Proceedings of the 46th Aerospace Sciences Meeting and Exhibit*, Reno NV, 2008.

[9]Mani, K. and Mavriplis, D. J., "Geometry Optimization in Three-Dimensional Unsteady Flow Problems using the Discrete Adjoint," *AIAA Paper 2013-0662, 51st AIAA Aerospace Sciences Meeting*, Grapevine, TX, January 2013.

[10]Mishra, A., Mani, K., Mavriplis, D. J., and Sitaraman, J., "Time-dependent Adjoint-based Aerodynamic Shape Optimization Applied to Helicopter Rotors," *Journal of Computational Physics*, Vol. 292, No. 1, 2015, pp. 253–271, doi:10.1016/j.jcp.2015.03.010.

[11]Menter, F. R., "Two-equation eddy-viscosity turbulence models for engineering applications," *AIAA journal*, Vol. 32, No. 8, 1994, pp. 1598–1605.

[12]Wilcox, D. C., "Formulation of the kw turbulence model revisited," *AIAA journal*, Vol. 46, No. 11, 2008, pp. 2823–2838.

[13]Mavriplis, D. J., "Unstructured-Mesh Discretizations and Solvers for Computational Aerodynamics," *AIAA Journal*, Vol. 46-6, June 2008, pp. 1281–1298.

[14]Mavriplis, D. J., "Multigrid Strategies for Viscous Flow Solvers on Anisotropic Unstructured Meshes," *Journal of Computational Physics*, Vol. 145, No. 1, Sept. 1998, pp. 141–165.

[15]Bridges, J. and Brown, C. A., "Parametric Testing of Chevrons on Single Flow Hot Jets," *AIAA Paper 2004-2824, 10th AIAA/CEAS Aeroacoustic Conference*, Manchester, GB, May 2004.

[16]Tanna, H. K., Dean, P. D., and J., F. M., "The Influence of Temperature on Shock-Free Supersonic Jet Noise," *Journal of Sound and Vibration*, Vol. 39, No. 4, 1975, pp. 429–460.

[17]Dippold, V. F., "Generating a Grid for Unstructured RANS Simulations of Jet Flows," *AIAA Paper 2018-3223, 2018 Fluid Dynamics Conference*, Atlanta, GA, June 25–29 2018, p. 3223.

[18]Fabiano, E., Mishra, A., Yang, Z., and Mavriplis, D. J., "Towards Adjoint-based Sensitivity Analysis for Supersonic Jet Noise," *AIAA Paper 2020–3131, AIAA Aviation 2020 Forum (virtual)*, June 15–19 2020.

[19]Yang, Z. and Mavriplis, D. J., "A Mesh Deformation Strategy Optimized by the Adjoint Method on Unstructured Meshes," *AIAA Journal*, Vol. 45, No. 12, 2007, pp. 2885–2896.

[20]Mavriplis, D. J., Yang, Z., and Long, M., "Results using NSU3D for the first Aeroelastic Prediction Workshop," *AIAA Paper 2013–0786, 51st Aerospace Sciences Meeting*, Grapevine, TX, 2013.

[21]Brazell, M. J., Sitaraman, J., and Mavriplis, D. J., "An overset mesh approach for 3D mixed element high-order discretizations," *Journal of Computational Physics*, Vol. 322, 2016, pp. 33–51.

[22]Bonet, J. and Peraire, J., "An alternating digital tree (ADT) algorithm for 3D geometric searching and intersection problems," *International Journal for Numerical Methods in Engineering*, Vol. 31, No. 1, 1991, pp. 1–17.

[23]Leib, S. J. and Goldstein, M. E., "Hybrid Source Modeling for Predicting High-Speed Jet Noise," *AIAA Journal*, Vol. 49, 2011, pp. 1324–1335.

[24]Bridges, J., Khavaran, A., and Hunter, C. A., "Assessment of Current Jet Noise Prediction Capabilities," NASA/TM 2008-215275.

[25]Bridges, J., "Rapid Prediction of Installed Jet Noise from RANS," *AIAA Paper 2019-2732, 25th AIAA/CEAS Aeroacoustic Conference*, Delft, The Netherlands, May 20–23 2019.

[26]Engblom, W. A., Khavaran, A., and Bridges, J., "Numerical Prediction of Chevron Nozzle Noise Reduction using WIND-MGBK Methodology," *AIAA Paper 2004-2979, 10th AIAA/CEAS Aeroacoustic Conference*, Manchester, GB, May 2004.